CRF-BASED SEGMENTATION OF HUMAN TEAR MENISCUS OBTAINED WITH OPTICAL COHERENCE TOMOGRAPHY

Gabriel Tsechpenakis[1], Jianhua Wang[2]

[1]Electrical & Computer Eng. Dept., University of Miami, FL 33134
Email: gavriil@miami.edu, Tel: (+1) 305-284 3340
[2]Department of Ophthalmology, Bascom Palmer Eye Institute, University of Miami, FL 33136
Email: jwang3@med.miami.edu, Tel: (+1) 305-482 5010

ABSTRACT

The dynamic variation of the human tear meniscus (tears around the eye lids) is very critical in visual function, maintenance of corneal integrity, and ocular comfort. The quantitative measuring of the tear menisci around the eyelids is though a challenging task. In our work, tear meniscus images are obtained with our custom-built Optical Coherence Tomography (OCT) and are processed using our novel segmentation method. For the latter, we use an implicit deformable model driven by a Conditional Random Field (CRF). The evolution of the model is solved as MAP estimation. The target conditional probability is decomposed using a simple graphical model, where the probability field of the pixel labels given the image observations is estimated using a discriminative CRF. Our results show that our segmentation approach successfully handles clutter and boundary ambiguities of the tear menisci, which makes our integrated system reliable for the every day medical practice.

Index Terms— Optical Coherence Tomography, Tear Meniscus, CRF-based segmentation, deformable models.

1. INTRODUCTION

When tears are secreted by the lacrimal gland, they are distributed into the cul-de-sac (about 4.5 µl), the tear menisci (about 2.9 µl), and pre-ocular tear film (about 1.1 µl) [13]. Some of the tear drains into the drainage system (via the puncta) or evaporates into the air. The volume is maintained in a dynamic balance among all aspects of the tear cycle. The tears are reserved at the edge of the eyelids forming tear menisci and cul-de-sac for the deposition on the ocular surface (forming the tear film). Upper tear meniscus is the tears around the edge of upper eyelid and lower tear meniscus is the tears around the lower eyelid.

Any malfunction or disturbance of any aspect of the tear cycle, from secretion to drainage, will compromise the
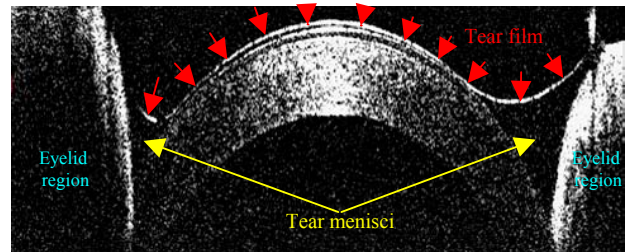
Fig. 1. Optical Coherence Tomography (OCT): an instance of the tear film (red arrows) and the tear menisci (yellow arrows).

integrity of the tear film and potentially cause ocular discomfort and diseases [11]. Attempts to research the fundamental properties of the tear film cycle have included the quantitative structure of the tear film [17], the deposition of the tear film by a blink [18], its redistribution after a blink [2], and the formation of dry spots [4]. The tear menisci, around the eyelids, change during and between blinks. Because it is extremely difficult to measure these tear parameters at the same time and because these variables vary widely from person to person based on physiological conditions, attempts to characterize the tear dynamics using any traditional method have proved elusive.

Optical Coherence Tomography (OCT) is an imaging modality based on the magnitude of backscattered light reflected from target tissues [3]. This quick, non-contact and non-invasive method has been intensively used *in vivo* and *in vitro* for analysis of the posterior segment of the eye, including thickness measurements of the retina and nerve fiber layers in various conditions [1]. Based on our previous work [8], we built a custom OCT to measure the variation of the tear menisci. The goal of this study is the automated segmentation of the tear menisci in OCT images, and our novel approach belongs to a specific category, namely the deformable models.

### 1.2. Previous Work on Segmentation

Parametric deformable models [7] use parametric curves to represent the model shape; starting from an initial estimate, they move towards the desired region of interest (ROI)

boundaries using image-driven and curve-smoothing (internal) forces. Most of these models use image edges to attract the curve towards the desired boundaries, which makes them less robust to noise, background complexity, and boundary ambiguities. Other parametric methods use region-based features [16], but they do not update the region statistics during the model evolution (local feature variations are difficult to be captured). Another category of deformable models is the implicit geometric models [14], which use the level-set based shape representation. Some of these methods integrate boundary and region-based information [15]; however, these frameworks assume piecewise or Gaussian intensity distributions within each partitioned image region, which limits their ability to capture intensity inhomogeneities and complex intensity distributions. To tackle this problem, another class of deformable models were proposed in [5], namely the Metamorphs, which uses both edge and texture information in a semi-parametric model. Among the parametric and implicit deformable models, and apart from the traditional energy minimization, there are methods that convert the energy-driven model evolution into a maximum a posteriori (MAP) problem, using a probabilistic formulation. In the survey of [12], methods that use probabilistic formulations are described. The main drawback of most of these methods is that they use only edge information, although they are more robust than similar deterministic approaches. In [6] the integration of probabilistic deformable models with Markov Random Fields (MRFs) in a graphical framework was proposed to overcome the limitations of edge-based probabilistic methods: the results show that the use of MRFs outperforms methods that do not use smoothing in the label field. As an alternative to the MRFs, and to obtain better smoothing in the probability (or label) fields, Conditional Random Fields (CRFs) were introduced in computer vision [10]. Although CRFs were first used to label sequential data, extensions of them were used for image segmentation [9]. The main advantage of CRFs, compared to MRFs, is that they handle the known label bias problem [10], incorporating spatial neighborhood dependencies in both the labels and the image features; also, for binary pixel classification, the MAP inference is computationally tractable (e.g., using graph min-cut algorithms).

In this work we use a probabilistic implicit deformable model that combines the advantages of the above approaches: (i) topology independence, (ii) updating of the model interior statistics, (iii) robustness, using a MAP formulation of the problem, and (iv) we exploit the superiority of CRFs compared to MRFs for image segmentation, coupling a CRF with the deformable model.

2. OUR SEGMENTATION APPROACH

We use an implicit representation of the evolving curve and we follow a probabilistic formulation of the energy terms,
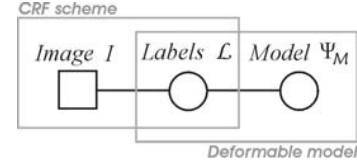
Fig. 2. Graphical model for the integration of the CRF in the implicit deformable model.

namely the image-driven and the smoothness term. Using the simple graphical model of Fig. 2, we integrate the deformable model with a CRF scheme; then, the energy minimization is solved as a MAP problem.

Let M be the deformable model, i.e., the evolving front that separates the model ROI R_M from the background $\Omega \backslash R_M$, where Ω indicates the image domain. We represent the model shape implicitly with the distance function

$$\Phi_M(\mathbf{x}) = \begin{cases} 0, \mathbf{x} \in M \\ + d(\mathbf{x}, M), \mathbf{x} \in R_M \\ - d(\mathbf{x}, M), \mathbf{x} \in \Omega \backslash R_M \end{cases} \quad (1)$$

where $\mathbf{x} = (x,y)$ is the pixel location in Cartesian coordinates and $d(\mathbf{x},M)$ denotes the minimum Euclidean distance from the pixel location $\mathbf{x}$ to the model M.

We formulate the segmentation problem as a joint MAP estimation problem:

$$\left\langle \Phi_M^*, L^* \right\rangle = \underset{(\Phi_M, L)}{arg\,max}\, P(\Phi_M, L \mid I) \quad (2)$$

where L is the set of the pixel labels, i.e., $L = \{$ ROI, background $\}$, and I is the input image. According to the graphical model of Fig. 2, the probability $P(\Phi_M, L \mid I)$ is decomposed into,

$$P(\Phi_M, L \mid I) = P(\Phi_M) \cdot P(I) \cdot P(L \mid \Phi_M) \cdot P(L \mid I) \quad (3)$$

The image prior $P(I)$ is expressed in terms of the gaussian distribution,

$$P(I(\mathbf{x}_i)) = \frac{1}{\sqrt{2\pi\sigma_0^2}} exp\left\{ -\frac{[I(\mathbf{x}_i)]^2}{\sigma_0^2} \right\} \quad (4)$$

where $I(\mathbf{x}_i)$ is the intensity of the pixel $\mathbf{x}_i$.

The conditional probability $P(L \mid \Phi_M)$ is formulated as the softmax function,

$$P(l_i \mid \Phi_M) = \frac{1}{1 + exp\{- \Phi_M(\mathbf{x}_i)\}} \quad (5)$$

where l_i is the label associated to the pixel $\mathbf{x}_i$. The effect of the above expression is that the probability of a pixel belonging to the ROI reduces dramatically outside the model, while it approaches 1 in the model interior.

The model prior $P(\Phi_M)$ is a probabilistic formulation of the model internal energy (smoothness term). We define the model internal energy in terms of the area of the model interior, and the first derivative of the model distance transform,

$$E_{int}(M) = \varepsilon_1 \cdot A(R_M) + \varepsilon_2 \iint_{\partial R_M} \|\nabla \Phi_M(x)\| dx, \quad (6)$$

where ε_1, ε_2 are weighting constants, $A(R_M)$ denotes the area of the model interior, and ∂R_M denotes a narrow band around the model. The minimization of the above energy forces the model to the position with the minimum interior area and the maximum smoothness along the model. (Note that $\nabla\Phi_M$ is defined $\forall \mathbf{x} \in \Omega$, and it is used in a similar manner as in the Mumford-Shah formulation [14]). Thus, we can express the model prior using the gibbs distribution,

$$P(\Phi_M) = \frac{1}{z} exp\{-E_{int}(M)\} \qquad (7)$$

The remaining term $P(\,L\mid I\,)$ of eq. (3) that associates the label field (pixel labels) with the image intensity is estimated using the CRF described below.

2.1. The Discriminative CRF

We use the discriminative formulation of the CRFs of [9]. Let $L = \{\,l_i\,\}$ be the labels associated to the image pixels; in our case, a label can have two values, *i.e.*, a pixel belongs to the model interior or the exterior (background). The discriminative CRF can estimate directly the labels distribution given an appropriate set of image features as,
$$p(L\mid I) =$$

$$\frac{1}{Z} exp\left\{\sum_{i\in\|\Omega\|}\psi_a(l_i, I(\mathbf{x}_i)) + \sum_{i\in\|\Omega\|}\sum_{j\in N_i}\psi_{in}(l_i, l_j, I(\mathbf{x}_i), I(\mathbf{x}_j))\right\} \quad (8)$$

where Z is a normalization constant, $\|\Omega\|$ is the size of the image domain, and N_i indicates the neighborhood of the i-th pixel. In this definition, ψ_a is called *association potential*, since it *associates* the label of a pixel with its intensity. Also, ψ_{in} is called *interaction potential*, since it determines the *interaction* between the neighboring pixels, in terms of both their intensity values and their labels. Note that common MRFs can be expressed in terms of an association and interaction potential, with the difference that in MRFs only the interactions between labels are taken into account in the interaction potential (which causes the known label bias problem [10]).

The association potential of eq. (8) is defined as the log likelihood,

$$\psi_a(l_i, I(\mathbf{x}_i)) = log\,P(l_i\mid I(\mathbf{x}_i)) \qquad (9)$$

whereas the interaction potential between two neighboring pixels is given by,
$$\psi_{in}(l_i, l_j, I(\mathbf{x}_i), I(\mathbf{x}_j)) =$$

$$\frac{1}{z_{in}} exp\left\{\frac{\delta(l_i - l_j)}{\sigma^2}\right\}\cdot\|I(\mathbf{x}_i) - I(\mathbf{x}_j)\| \qquad (10)$$

where z_{in} is a normalization constant. The interaction potential is responsible for smoothing the probability field defined in eq. (8), if two neighboring pixels have different intensity values; otherwise the interaction potential has no effect.

2.2. The Segmentation Algorithm in Steps

The overall algorithm for the model evolution consists of the following steps:
(i)   Model initialization and learning of the ROI statistics (log likelihood of eq. (9)) from both training samples and the model interior.
(ii) Estimation of the probability field $P(L\mid I)$ from step (i), independently for each pixel.
(iii) Estimation the association and interaction potentials, according to eqs. (9), (10), and estimation of the smoothed probability field of eq. (8).
(iv) Evolution of the model within a band around it, based on eq. (2): we use the decomposition of eq. (3) and we replace the probabilities with the definitions of eqs. (4), (5), (7) and (8).
(v)   For the new position of the model, update the interior statistics and repeat the steps (iii) and (iv).

3. EXPERIMENTAL RESULTS

To evaluate the performance of our tear menisci segmentation method, we compared the menisci areas (i) extracted manually, which served as ground-truth, (ii) using six points (placed manually) on the menisci boundaries, which was used previously as evaluation approach, and (iii) estimated after segmenting the tear menisci using our approach. The resolution of the images obtained from our OCT is 384x960 pixels.

As ground-truth, we placed manually several points around the tear menisci to obtain accurate boundaries. For the specific OCT image shown in Fig. 3, the areas of the left and right menisci were 4,562 and 16,695 pixels respectively. According to the evaluation approach we used to follow previously, placing 6 points on the menisci boundaries (Fig. 3), the areas of the left and right menisci were 5,215 and 18,936 pixels, respectively. Finally, after segmenting the menisci automatically, using our method (Fig. 4), the estimated areas of the left and right menisci were 4,112 and 16,037 pixels respectively. These results are summarized in Table 1. Clearly, our approach gives more accurate results from our previous manual evaluation and close to the ground-truth. Finally, from Fig. 4 one can see that our method can estimate the menisci boundaries even where there are boundary and region ambiguities, as well as local variations in the region features (intensity distributions).

| Tear meniscus	Left (pixels)	Right (pixels)
Ground-truth	4,562	16,695
6-point evaluation	5,215	18,936
Our method	4,112	16,037

Table 1. Area estimation (in pixels) using (i) ground-truth boundaries, (ii) our previous 6-point evaluation (manual), and (iii) our novel segmentation method.

4. CONCLUSIONS

The automatic quantitative estimation of the tear menisci around the eyelids is a challenging task. Using our custom-built OCT, we can obtain images for monitoring the tear film and menisci. In this paper, we presented our novel method for segmenting the tear menisci in a robust and accurate way. Our method uses an implicit deformable model and a CRF, tightly coupled in a graphical model, and the boundaries are obtained as the solution of a MAP problem. Our results, qualitative (figures) and numerical (estimated areas), show that our method can be used reliably in every-day medical practice.

5. REFERENCES

[1] R.J. Antcliff, M.R. Stanford, D.S. Chauhan, et al., "Comparison between optical coherence tomography and fundus fluorescein angiography for the detection of cystoid macular edema in patients with uveitis," *Ophthalmology*. 107:593-599, 2000.

[2] S.I. Brown, D.G. Dervichian, "Hydrodynamics of blinking. In vitro study of the interaction of the superficial oily layer and the tears," *Arch Ophthalmol*.82:541-547, 1969.

[3] J.G. Fujimoto, S.A. Boppart, G.J. Tearney, B.E. Bouma, C. Pitris, M.E. Brezinski, "High resolution *in vivo* intra-arterial imaging with optical coherence Tomography," *Heart*, 82:128-133, 1999.

[4] F. Holly, "Formation and stability of the tear film," *International Ophthalmology Clinics*, 13:73-96, 1973.

[5] X. Huang, D. Metaxas, and T. Chen, "Metamorphs: Deformable Shape and Texture Models," *IEEE Conference on Computer Vision and Pattern Recognition*, 2004.

[6] R. Huang, V. Pavlovic, and D. Metaxas, "A Graphical Model Framework for Coupling MRFs and Deformable Models," *IEEE Conference on Computer Vision and Pattern Recognition*, 2004.

[7] M. Kass, A. Witkin, and D. Terzopoulos, "Snakes: Active contour models," *Int'l Journal of Computer Vision*, 1:321-331, 1987.

[8] P.E. King-Smith, B.A. Fink, N. Fogt, K.K. Nichols, R.M. Hill, G.S. Wilson, "The thickness of the human precorneal tear film: evidence from reflection spectra," *Invest Ophthalmol Vis Sci*., 41:3348-3359, 2000.

[9] S. Kumar and M. Hebert, "Discriminative Random Fields: A Discriminative Framework for Contextual Interaction in Classification," *IEEE International Conference on Computer Vision*, 2003.

[10] J. Lafferty, A. McCallum, and F. Pereira, "Conditional Random Fields: Probabilistic Models for Segmenting and Labeling Sequence Data," *Eighteenth International Conference on Machine Learning*, 2001.

[11] M.A. Lemp, F.J. Holly, S. Iwata, C.H. Dohlman, "The precorneal tear film. I. Factors in spreading and maintaining a continuous tear film over the corneal surface," *Arch Ophthalmol,* 83:89-94, 1970.

[12] T. McInerney and D. Terzopoulos, "Deformable Models in Medical Image Analysis: A Survey," *Medical Image Analysis*, 1(2), 1996.
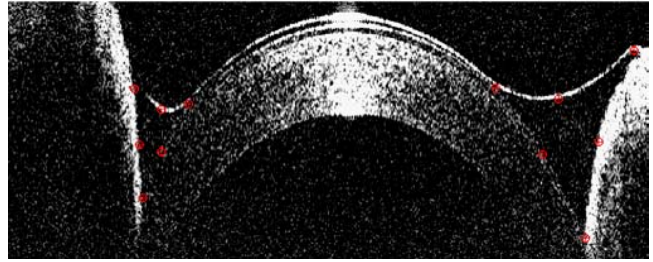
Fig. 3. Image obtained by our custom built OCT: previously, the points (in red) were placed manually on the image to estimate the tear menisci areas.
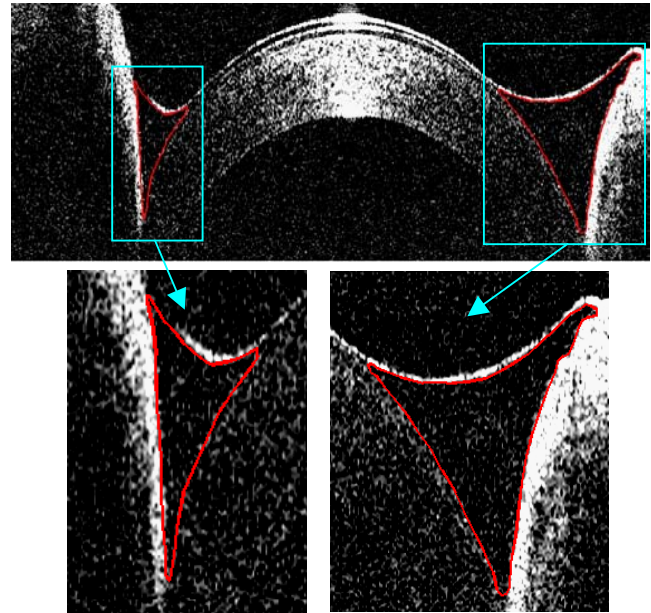
Fig. 4. Our results for the segmentation of the tear menisci in the OCT image: the estimated boundaries are shown with red lines.

[13] S. Mishima, A. Gasset, S.D. Klyce, J.L. Baum, "Determination of tear volume and tear flow," *Investigative Ophthalmology*," 5:264-276, 1966.

[14] D. Mumford and J. Shah, "Optimal Approximations by Piecewise Smooth Functions and Associated Variational Problems," *Communications on Pure and Applied Mathematics*, 42(5):577-685, 1989.

[15] N. Paragios and R. Deriche, "Geodesic Active Regions and Level Set Methods for Supervised Texture Segmentation," *Int'l Journal of Computer Vision*, 46(3):223247, 2002.

[16] R. Ronfard, "Region-based strategies for active contour models," *International Journal of Computer Vision*, 13(2):229-251, 1994.

[17] E. Wolff, "Mucocutaneous junction of lid-margin and distribution of tear film fluid," *Trans Am Ophthalmol Soc*., 66:291-308, 1946.

[18] H. Wong, I. Fatt, C. Radke, "Deposition and thinning of the human tear film," *J Colloid Interface Sci*., 184:44-51, 1996.